



Title	Numerical weather prediction system based on JMA-NHM for field observation campaigns on the Greenland ice sheet
Author(s)	Hashimoto, Akihiro; Niwano, Masashi; Aoki, Teruo; Tsutaki, Shun; Sugiyama, Shin; Yamasaki, Tetsuhide; Iizuka, Yoshinori; Matoba, Sumito
Citation	低温科学, 75, 91-104
Issue Date	2017-03-31
DOI	10.14943/lowtemsci.75.91
Doc URL	http://hdl.handle.net/2115/65105
Type	bulletin (article)
File Information	11_91-104.pdf



[Instructions for use](#)

Numerical weather prediction system based on JMA-NHM for field observation campaigns on the Greenland ice sheet

Akihiro Hashimoto^{1*}, Masashi Niwano¹, Teruo Aoki^{2,1}, Shun Tsutaki³, Shin Sugiyama⁴, Tetsuhide Yamasaki⁵, Yoshinori Iizuka⁴, Sumito Matoba⁴

Received 25 October 2016, accepted 11 January 2017

As part of a research project titled, "Snow Impurity and Glacial Microbe effects on abrupt warming in the Arctic" (SIGMA), numerous observation campaigns were conducted on the Greenland ice sheet (GrIS) from FY2011 to FY2015. To support research activities in the field, the Japan Meteorological Agency Non-Hydrostatic Model (JMA-NHM) was applied to form a numerical weather prediction system covering all of Greenland. Before executing our numerical simulation using this model, however, we modified the model to better represent the meteorological processes over the GrIS, since the original model was adjusted to fit mid-latitude environments. Using our modified model, we performed numerical weather prediction twice per day such that expedition crews in the field could access the resulting prediction information in the morning and evening, which helped them plan and execute their daily missions. Further, we improved our model during these campaigns by referencing the daily reports obtained from the observation site on the GrIS. In this paper, we describe our weather prediction system and evaluate its performance in reference to surface meteorological observation data.

Keywords: Greenland, Weather prediction, Non-hydrostatic model

1. Introduction

Field observation campaigns, especially in polar regions, often face severe weather conditions. Since weather is indeed one of the strongest factors that influence field activities, accurate weather prediction is crucial for making a campaign successful and ensuring the safety of the individuals involved. In general, operational weather predictions have limited availability in such campaign areas. There are research-based prediction systems that target polar regions, in particu-

lar the Arctic Numerical Weather Prediction (Hines et al., 2008, Hines et al., 2011, Wilson et al., 2011) and Antarctic Numerical Weather Prediction (Powers et al., 2003, Bromwich et al., 2013) systems, both currently based on the Polar Weather Research and Forecasting (WRF) model, though previously on the Polar Fifth-generation Mesoscale Model (MM5) (Bromwich et al., 2005).

Unfortunately, these existing systems are not customized for particular campaigns. If expedition crews in the field are able to access prediction

*Corresponding Author

e-mail : ahashimo@mri-jma.go.jp

1) Meteorological Research Institute, Japan Meteorological Agency, Tsukuba, Japan

2) Graduate School of Natural Science and Technology, Okayama University, Okayama, Japan

3) Earth Observation Research Center, Japan Aerospace Exploration Agency, Tsukuba, Japan

4) Institute of Low Temperature Science, Hokkaido University, Sapporo, Japan

5) Avangnaq, Takatsuki, Japan

information customized for their specific campaigns, their activities become safer and more efficient. Further, observation data obtained during a campaign often include information regarding various phenomena that go undetected by operational observation systems, thus these data are useful for validation and improving existing weather prediction models.

In the summer seasons of 2011–2015, the “Snow Impurity and Glacial Microbe effects on abrupt warming in the Arctic” (SIGMA) project conducted glaciological, meteorological, and biological observation campaigns in Greenland (Aoki et al., 2014; Niwano et al., 2015). To support these campaigns, we created a specific weather prediction system in the summer season of 2013, then extended our system for campaigns held in successive years (Hashimoto et al., 2016). Weather prediction information was also shared with other cooperative field activities in Greenland, including the following: field observations of aerosol and frost flower at Siorapaluk, northwestern Greenland (Hara et al., 2014; Matoba et al., 2014); glacier dynamics observations on Bowdoin Glacier (Sugiyama et al., 2015) as part of the Green Network of Excellence Arctic Climate Change Research Project (GRENE-Arctic, 2011–2015); glaciological and meteorological observations at the southeastern dome (SE-Dome) site in southeastern GrIS (Iizuka et al., 2016); and maintenance of the Greenland Climate Network (GC-Net) Automatic Weather Station (AWS) by the Institute for Snow and Avalanches Research (SLF), Swiss Federal Institute for Forest, Snow and Landscape Research (WSL).

In the present paper, we describe our weather prediction system based on Hashimoto et al. (2016), showing prediction performance as evaluated with reference to surface meteorological observation data obtained from several field campaigns.

2. Meteorological data at field campaign sites

As part of the SIGMA project, an AWS was installed in the summer season of 2012 at a point called SIGMA-A on the northwest GrIS at 1,490 m above sea level (a.s.l.) (Aoki et al., 2014; Niwano et al., 2015), as shown in Fig. 1 (b). This AWS continues to measure meteorological parameters, including air temperature, humidity, air

pressure, wind speed, and wind direction, as well as radiative properties, including downward and upward shortwave radiation and longwave radiation. Similarly, again shown in Fig. 1 (b), as part of the GRENE-Arctic project, an AWS (WXT520, Vaisala) was installed on the eastern flank of Bowdoin Glacier at 100 m a.s.l. to measure air temperature, humidity, air pressure, wind speed, and wind direction during expeditions conducted in the summers of 2013, 2014, and 2015.

Further, in a field campaign spanning from late May to early June 2015 at the SE-Dome at 3,170 m a.s.l., as shown in Fig. 1 (c), air temperature, humidity, air pressure, wind speed, and wind direction were measured using a handheld meteorological meter (Kestrel 4500 NW). Cloud types, cloud coverage, and visibility were also recorded via visual observations. Specific explanations of the meteorological measurements from SIGMA-A, Bowdoin Glacier, and the SE-Dome are provided by Aoki et al. (2014), Sugiyama et al. (2015), and Iizuka et al. (2016), respectively. We compared our prediction results with these observation results to evaluate the accuracy of our prediction system.

3. Model description

We applied the Japan Meteorological Agency Non-Hydrostatic Model (JMA-NHM, Saito *et al.*, 2006) to our numerical experiments, essentially the same configuration as that of the operational weather prediction system implemented in Japan, with the following exceptions. First, instead of the original configuration, which adopts a double-moment scheme only for cloud ice and a single-moment scheme for other hydrometeors (i.e., snow and graupel), we applied a double-moment bulk cloud microphysics scheme to predict both the mixing ratio and concentration of particles of solid hydrometeors (i.e., cloud ice, snow, and graupel) and a single-moment scheme to predict only the mixing ratio of particles of liquid hydrometeors (i.e., cloud water and rain).

Second, for ice crystal formation in the atmosphere, we adopted a temperature-dependent parameterization instead of one that depends on the super-saturation ratio for ice and the updraft velocity of a grid from the original configuration. Third, we turned off the ice-saturation adjustment scheme (Tao et al., 1989) in the original

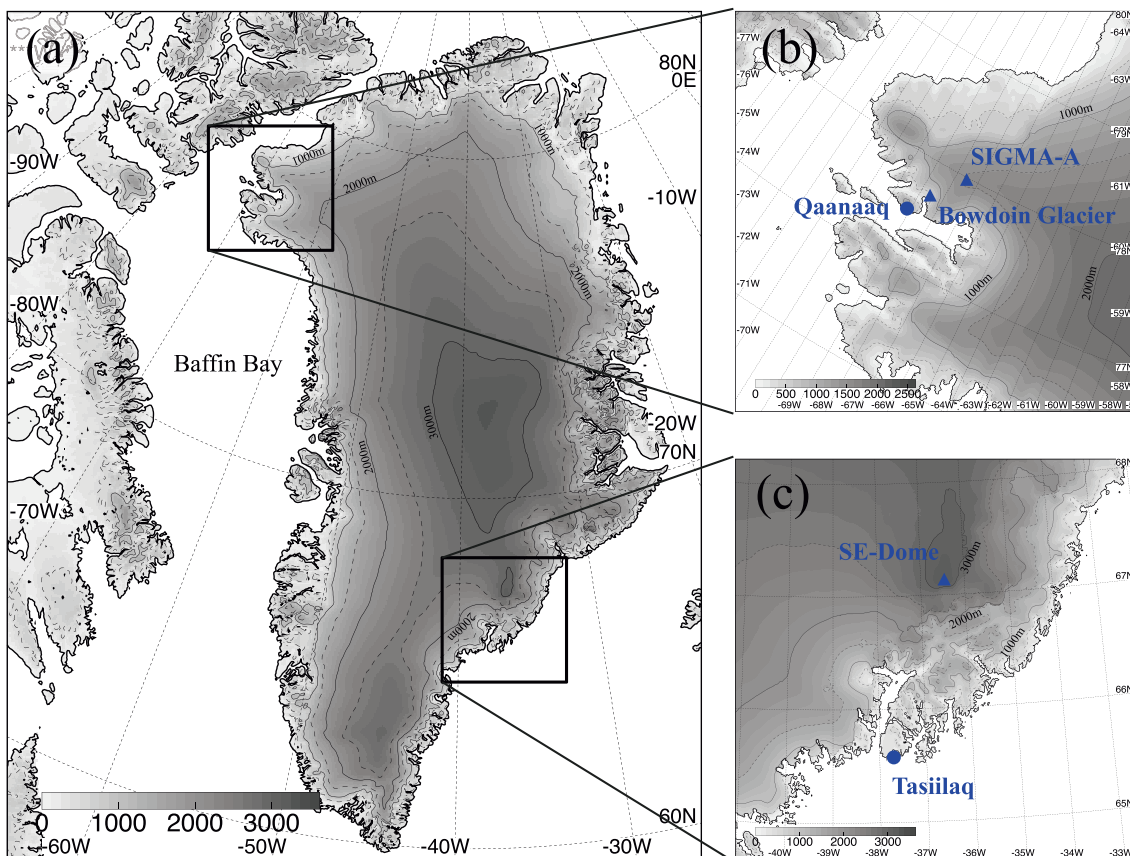


Figure 1 : (a) Calculation domain for our numerical weather prediction experiment, with enlarged views around (b) Qaanaaq and (c) Tasiilaq. Triangles and circles indicate camping sites and base towns, respectively.

configuration to avoid the unrealistic formation of ice clouds in the upper troposphere (Hashimoto et al. 2007). Similarly, we also turned off a cumulus parameterization.

JMA-NHM has four land surface classes, i.e., soil, snow, sea, and sea ice. In the original configuration, the surface temperature of a grid is allowed to rise higher than the freezing point even if the surface of the grid is classified as “snow”. Note that this considers the sub-grid scale heterogeneity of land surface characteristics (e.g., a mixture of soil and snow surface in a spatial scale less than the given grid spacing, i.e., several kilometers), which is usually included in domestic weather simulations (Hara, 2008). As our fourth alteration to the original model, we limited the surface temperature of a snow grid to be lower than the freezing point, since the heterogeneity of land surface characteristics is rarely seen on the GrIS.

4. Numerical experiments

Figure 1(a) shows the computational domain, with a

domain size of 2250×2750 km in the horizontal plane and 22 km in the vertical direction. Horizontal grid spacing is set at 5 km, while vertical grid spacing is stretched from 40 m at the surface to 886 m at the top of the domain. We employ 50 variable vertical layers using a terrain-following coordinate system. Integration time is 42 hours for each simulation, with a timestep interval between 8 and 12 seconds. Computations of the radiative process are performed every 15 minutes at a horizontal grid spacing of 20 km. The initial and boundary conditions were obtained from the global forecast obtained via the Global Spectral Model (GSM) of JMA. Model topography was based on the 5-km-mesh surface elevation data from the digital elevation model of Greenland provided by Bamber et al. (2001). Simulations were performed twice per day with an initial time of 06 or 18 UTC throughout the various campaigns, with hourly output data used for our analysis.

5. Results

5.1 SIGMA-A

Figure 2 shows the observed and predicted meteorological parameters throughout the field campaign period of July 2012 at SIGMA-A. The model did well in terms of predicting downward shortwave and longwave radiant fluxes, except for occasional under- or overestimations of a daily maximum of downward shortwave radiant flux, as shown in Fig. 2(a). When the observed shortwave radiation showed a clear sine curve, which indicates almost no cloud coverage, our predictions agreed with observations. Conversely, when cloudy conditions were expected, our predictions showed a bias from the observations. The mean error (ME) and root mean square error (RMSE) were -28.2 W m^{-2} and 69.9 W m^{-2} , respectively, for the predicted downward shortwave radiant flux, and -2.2 W m^{-2} and 23.9 W m^{-2} , respectively, for the predicted downward longwave radiant flux (Fig. A1 in Appendix A).

Aoki et al. (2014) reported that it rained intermittently from the afternoon of July 10, 2012 through the morning of July 13, 2012. The measurement of precipitation was performed from 18:00 local time on 12 July to 09:00 local time on 14 July during the event. The measured rainfall was 20 mm. Based on this value, the total amount of rainfall during the event was estimated to be 60–100 mm (Aoki et al., 2014). Niwano et al. (2015) estimated the total rainfall amount as 100 mm on the basis of ERA-Interim reanalysis data with appropriate correction. Appearance of this rainfall event was certainly predicted by our system, as indicated by the blue line in Fig. 2(a), but the total rainfall amount was predicted as 10 mm at the SIGMA-A site. In general, quantitative accuracy of rainfall prediction is affected by many factors, including a shift of rainfall zone. This point will be the subject of future study. The wind speed and direction, shown in Fig. 2(b), as well as the temperature and water vapor mixing ratio, shown in Fig. 2(c), showed generally good agreement between

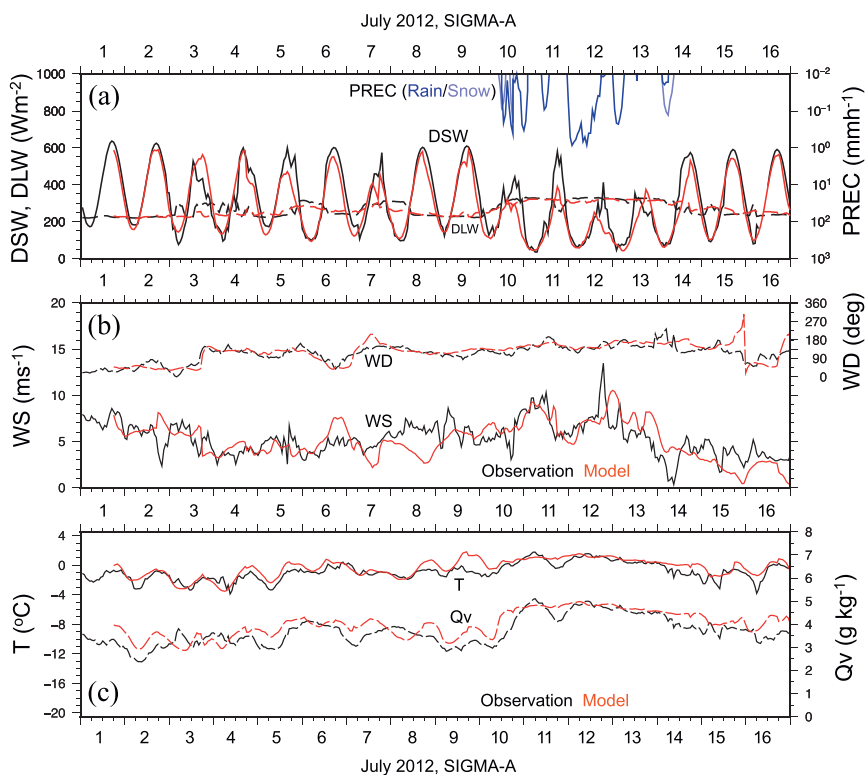


Figure 2 : (a) Observed (black) and predicted (red) downward shortwave (DSW, solid line) and longwave (DLW, broken line) fluxes at SIGMA-A for the campaign period of July 2012. (b) Same as (a), but solid and broken lines represent wind speed (WS) and direction (WD), respectively. (c) Same as (a), but solid and broken lines represent air temperature (T) and water vapor mixing ratio (Qv), respectively. Note that the blue line in (a) shows the predicted hourly precipitation amount.

observations and our predictions. According to the analysis of prediction error shown in Figs. A1 and A2(a)-(d), our prediction system has the same level of performance as in July 2012 throughout the campaigns in July 2013 (Fig. 3) and June 2014 (Fig. 4).

5.2 Bowdoin Glacier

Figure 5 shows the observed and predicted meteorological parameters through the field campaign period of July 2013 at Bowdoin Glacier (Sugiyama et al., 2015). Shown using solid lines in Fig. 5(a), the wind speed showed generally good agreement between observations and our predictions, although a large overestimation occurred in some cases. Our model showed a systematic bias in wind direction, as indicated by the red broken line in Fig. 5(a). An easterly wind was predicted by our model most of the time, while westerly winds were actually observed, except for a few short-lived occurrences of an easterly wind. This discrepancy in wind direction between observations and our predictions points to the existence of local circulations that are not resolved with a grid spacing of 5 km in our simulations. These same features appeared in our predictions during the 2014 and 2015 campaigns, as shown in Figs. 6 and 7, respectively.

Figure 6, however, revealed another feature. Between July 18, 2014 and July 22, 2014, a strong easterly wind of up to approximately 10 m s^{-1} was observed under the influence of a synoptic scale perturbation. During this period, in contrast with the other periods, our model accurately predicted both wind speed and direction. This remarkable turn for the better, accompanied by a strong wind, was also seen on July 25, 2013, as shown in Fig. 5. Figure 8 shows a scatter plot of the error of predicted wind direction and air temperature versus observed wind speeds. For 2013 and 2014, both Figs. 8(a) and 8(c) clearly indicate that the errors of predicted wind direction were never larger than 80 degrees when the observed wind speed was larger than 5 m s^{-1} .

For surface air temperature, our model showed a positive bias for most campaign periods in 2013 and 2015, as shown in Figs. 5(b) and 7(b), respectively, as well as better performance in 2014, as shown in Fig. 6(b). Figures 8(b), 8(d), and 8(f) provide scatter plots showing

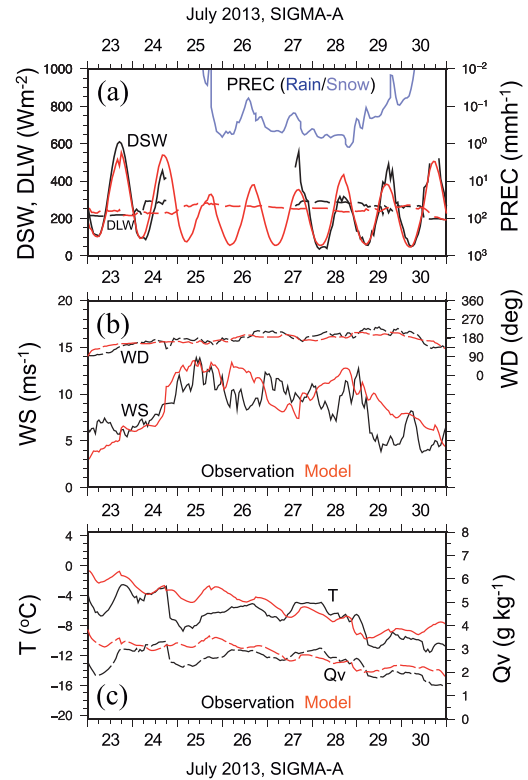


Figure 3 : Same as Fig. 1, but for the campaign period of July 2013.

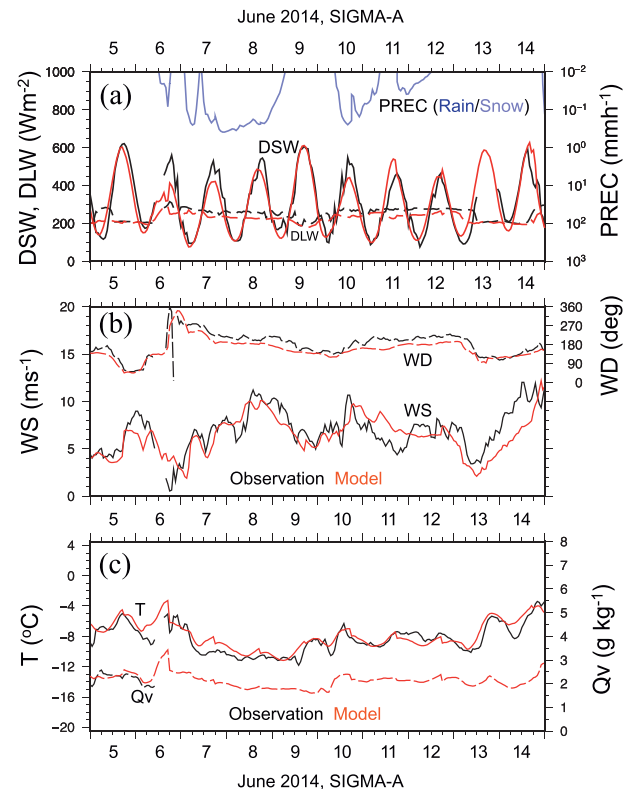


Figure 4 : Same as Fig. 1, but for the campaign period of June 2014.

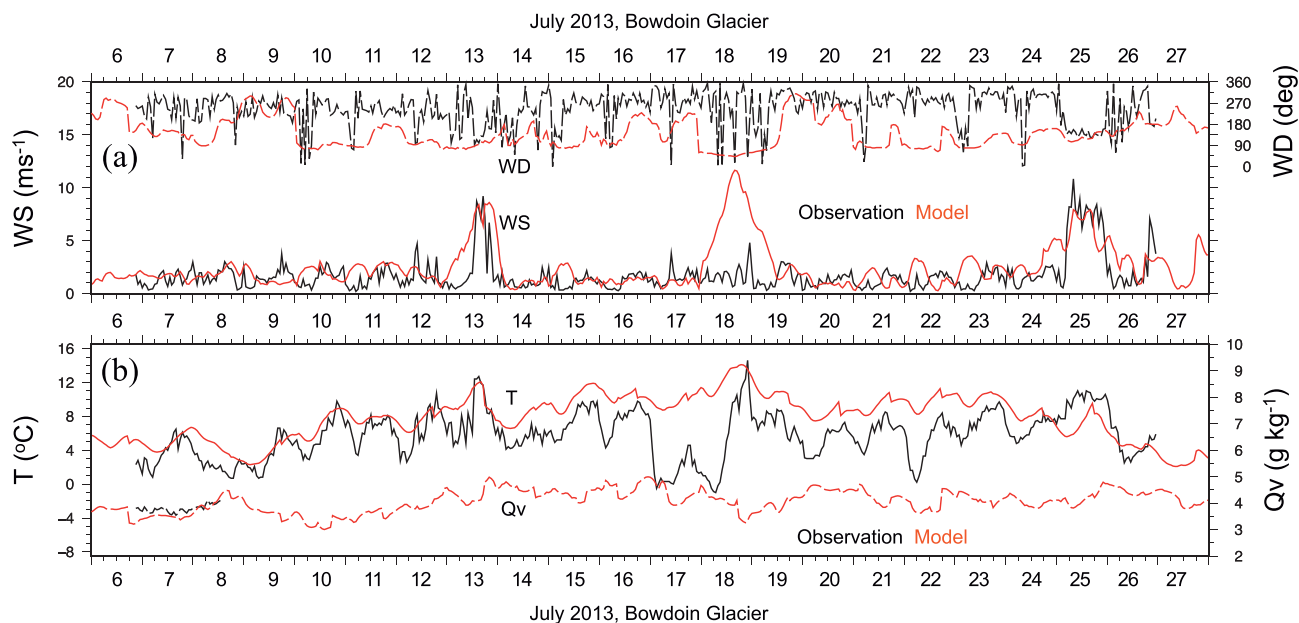


Figure 5 : (a) Observed (black) and predicted (red) wind speed (WS, solid line) and direction (WD, broken line) at Bowdoin Glacier for the campaign period of July 2013. (b) Same as (a), but solid and broken lines represent air temperature (T) and water vapor mixing ratio (Qv), respectively.

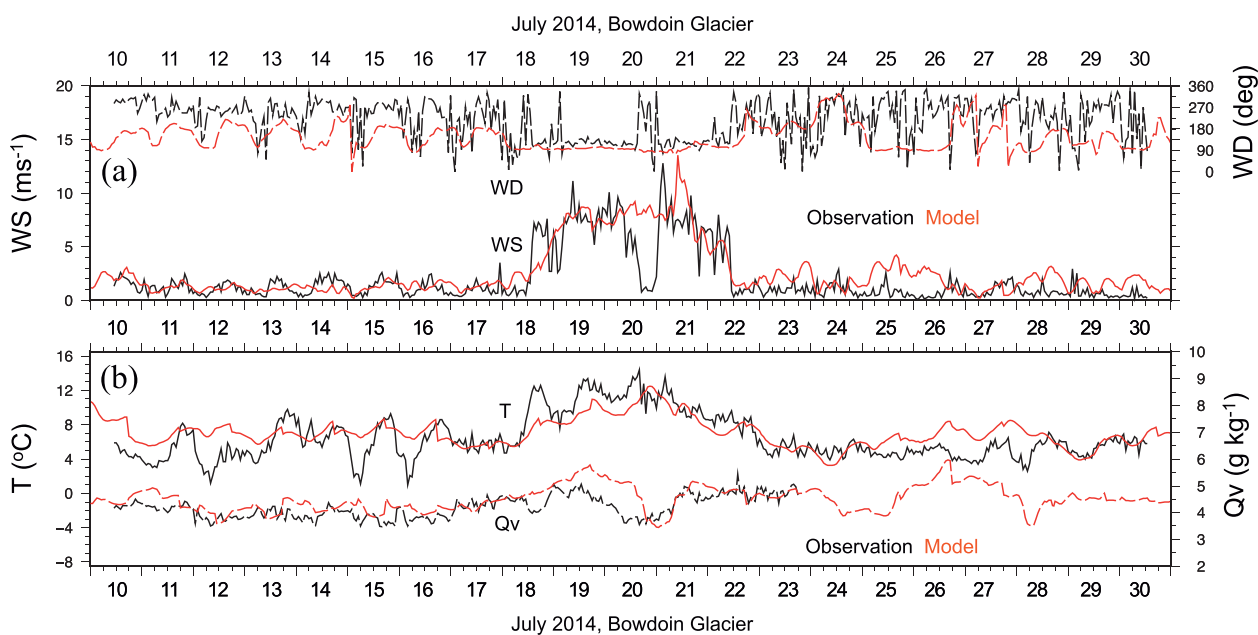


Figure 6 : Same as Fig. 4, but for the campaign period of July 2014.

the errors of predicted air temperature versus observed wind speeds. Similar to wind direction, predicted air temperatures tended to agree with observed values when the observed wind speed was greater than 5 m s^{-1} .

Finally, for the mixing ratio of water vapor, our simulated results agreed with observed results throughout the three field campaigns at Bowdoin Glacier, though note that there were periods of time in which measure-

ments were not available. The ME and RSME of predicted parameters at Bowdoin Glacier are summarized in Fig. A2(e)–(h) (Appendix A).

5.3 SE-Dome

Figure 9 shows observed and predicted wind speeds and surface air temperatures at the SE-Dome throughout an ice core drilling campaign conducted from May 19,

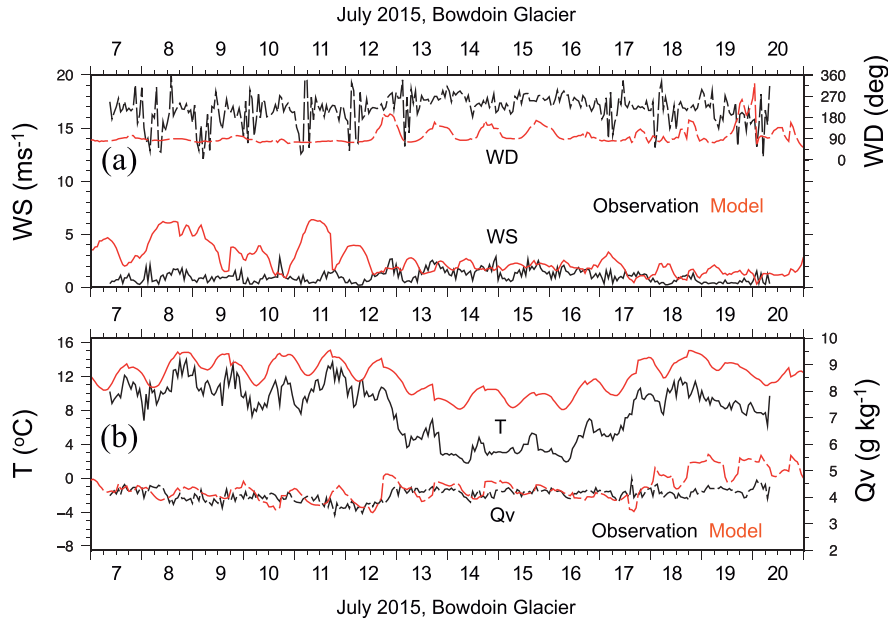


Figure 7 : Same as Fig. 4, but for the campaign period of July 2015.

2015 through June 2, 2015 (Iizuka et al., 2016). Our model accurately predicted strong winds of more than 10 m s^{-1} on May 20, May 29, and May 30, as shown in Fig. 9 (a), thus effectively warning the expedition team.

Conversely, predicted surface air temperatures showed defective behavior in that predicted values were much lower than observed values in the early predictions for each simulation, as is evident in Fig. 9(b). After examining our prediction system, we found a problematic procedure in the initiation of snow surface temperature. To correct the procedure, we provided an initial surface air temperature to initiate snow surface temperature. This correction yielded substantial improvements to our air temperature predictions, as shown in Fig. 9(d), without negatively impacting the accuracy of wind speed predictions, as is evident in Fig. 9(c). Note that we also updated the prediction system accordingly for the subsequent field campaign at Bowdoin Glacier in July 2015.

6. Discussion

6.1 Transmission of prediction results

When the expedition team stays at a nearby base town (e.g., Qaanaq for the SIGMA and GRENE-Arctic projects and Tasiilaq for SE-Dome campaigns), they can browse visualized prediction results through the

Internet; however, after leaving the base town for the camping site, the Internet is not available. A commercial satellite communication service is the only way to access weather information. Since satellite communication services are too expensive and have bit rates that are too small to use for obtaining large-scale images of weather prediction maps, our prediction results were translated into short documents and transmitted via e-mails through the satellite communication system.

When a research team had a weather analysis crew, in addition to the short document noted above, we also provided downsized data constructed by the procedure of Hashimoto et al. (2016) (see Appendix B for details). The crew retrieved prediction results from this data and shared them with the team. This means of transmission introduced only light loading on satellite communication, but was effective in updating the crew with necessary weather prediction information.

6.2 Effectiveness in field campaigns

Figure 10 shows the time evolution of sea level pressure based on the JMA's global objective analysis during the field campaign at SIGMA-A from July 24, 2013 through July 29, 2013. With the approach of an Arctic cyclone heading toward northern Greenland, Greenland high pressure weakened until its intensity started to recover after July 28, 2013. During this

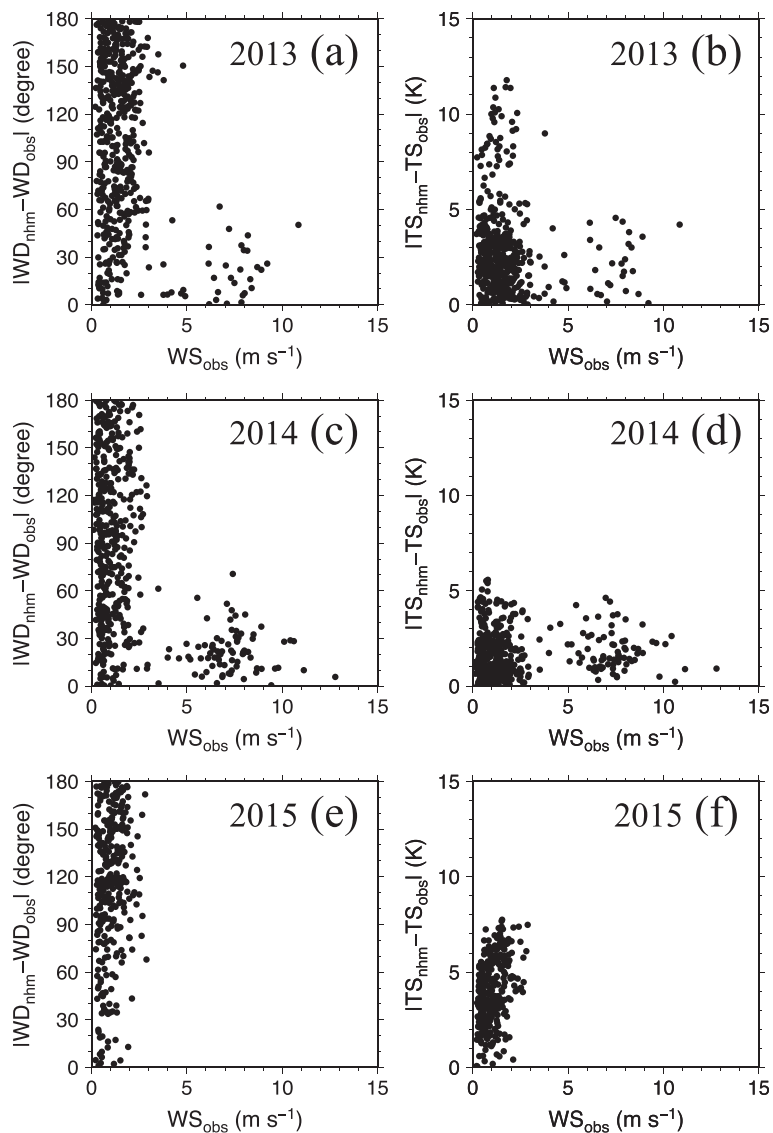


Figure 8 : Scatter plot of the error of (a) predicted wind direction and (b) predicted surface air temperature versus the observed wind speed in the 2013 field campaign at Bowdoin Glacier. Here (c) and (d), as well as (e) and (f), represent the same results as those of (a) and (b), but for the 2014 and 2015 field campaigns, respectively.

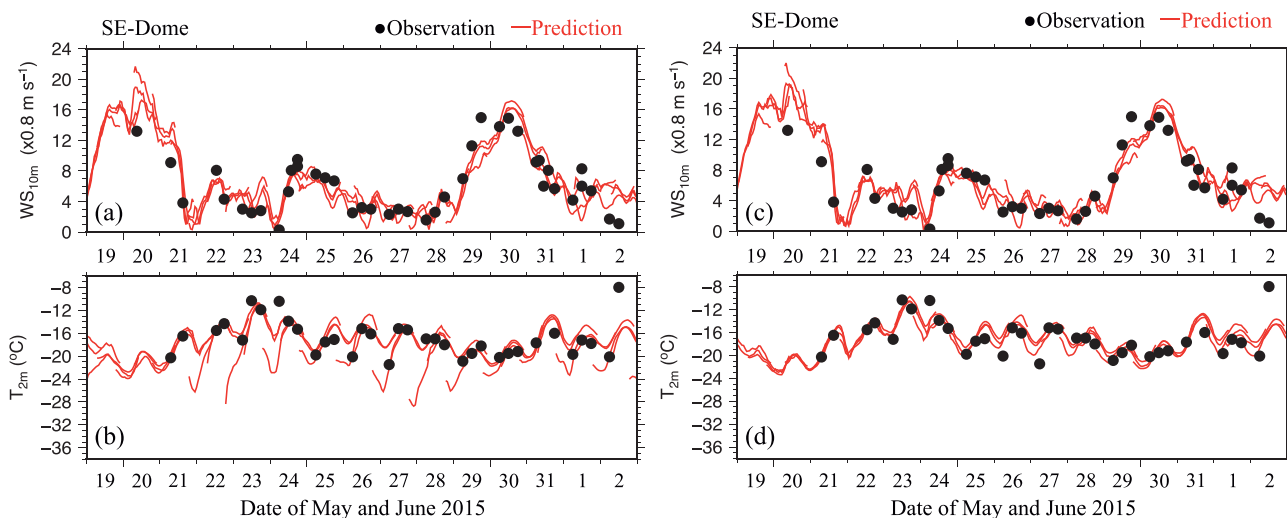


Figure 9 : (a) Observed (black dot) and predicted (red line) wind speed at the SE-Dome through the campaign period ranging from May 2015 through June 2015. (b) Same as (a), but for surface air temperature.

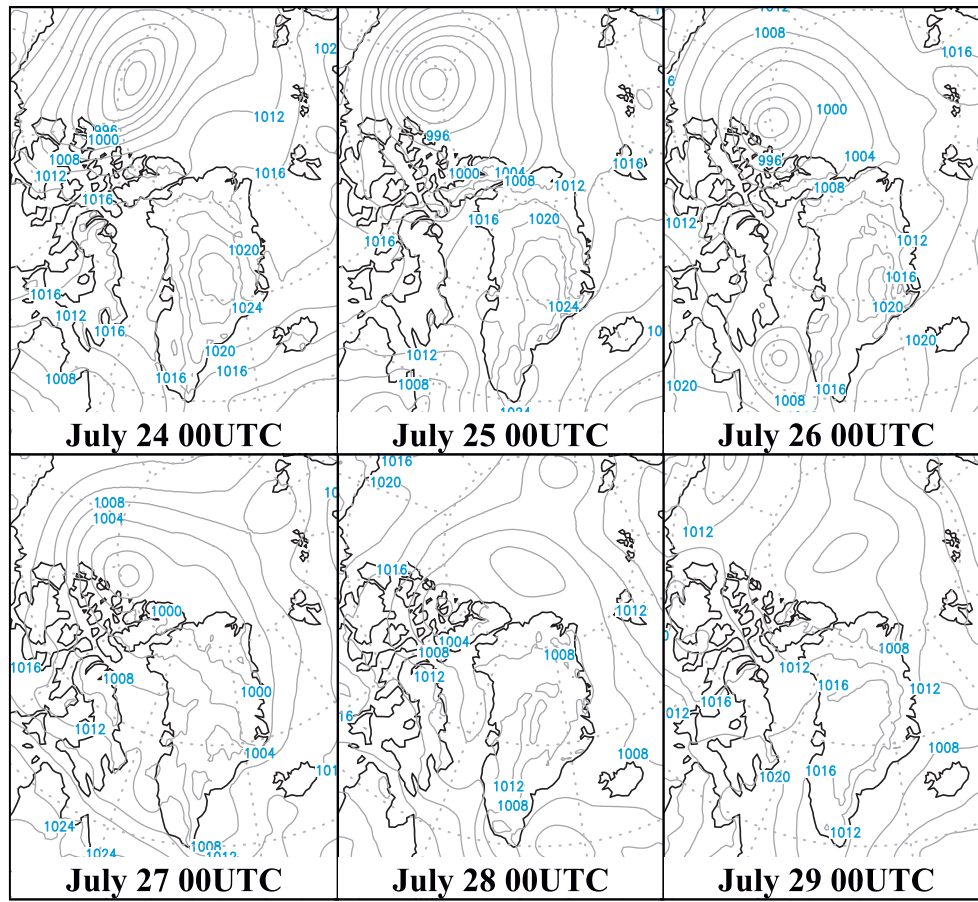


Figure 10 : Time evolution of sea level pressure from July 24, 2013 through July 29, 2013.

period, the expedition team experienced a blizzard at SIGMA-A, which forced them to cancel some of their scheduled measurements (Aoki et al., 2014). As shown in Fig. 3(b), our prediction system accurately predicted strong winds of up to approximately 10 m s^{-1} intermittently from July 25, 2013 through July 28, 2013. These predictions helped the crew shift their plans for taking measurements and schedule a helicopter flight back to the base town of Qaanaaq.

In the field campaign at the SE-Dome in late May through early June 2015 (Iizuka et al., 2016), the crew successfully flew to the camping site on May 18, 2015, one day before a heavy storm hit the site, accompanied by an Icelandic low. Using predictions produced by our prediction system, the crew felt they would encounter strong winds of up to 20 m s^{-1} the next day, as indicated in Fig. 9(a). In a strategic sense, they gained time to prepare their ice core drilling operations at the site, owing to the flight on May 18, 2015. They started the drilling operation on May 21, 2015, soon after the storm

left the site, thus completing all scheduled field studies on May 27, 2015. Unfortunately, for their flight back to their base town of Tasilaq, they were stuck until June 2, 2015 due to another storm accompanied by an Icelandic low that was closest to the SE-Dome on May 30, 2015, as shown in Fig. 11. The pick-up flight was then done after the weather improved, which was accurately predicted by our prediction system, as shown in Fig. 9(a).

The field campaigns in Greenland depended on heliborne transportation, which is vulnerable to such weather conditions as strong winds, low visibility, and insufficient clearance from the surface of ice sheets to a cloud base, and so on. Through the use of our numerical weather prediction system during the campaigns, our results show the effectiveness of our prediction system for scheduling heliborne transportation and for supporting the safe collection of scientific measurements.

6.3 Implications to modeling

As shown by the comparisons between observed

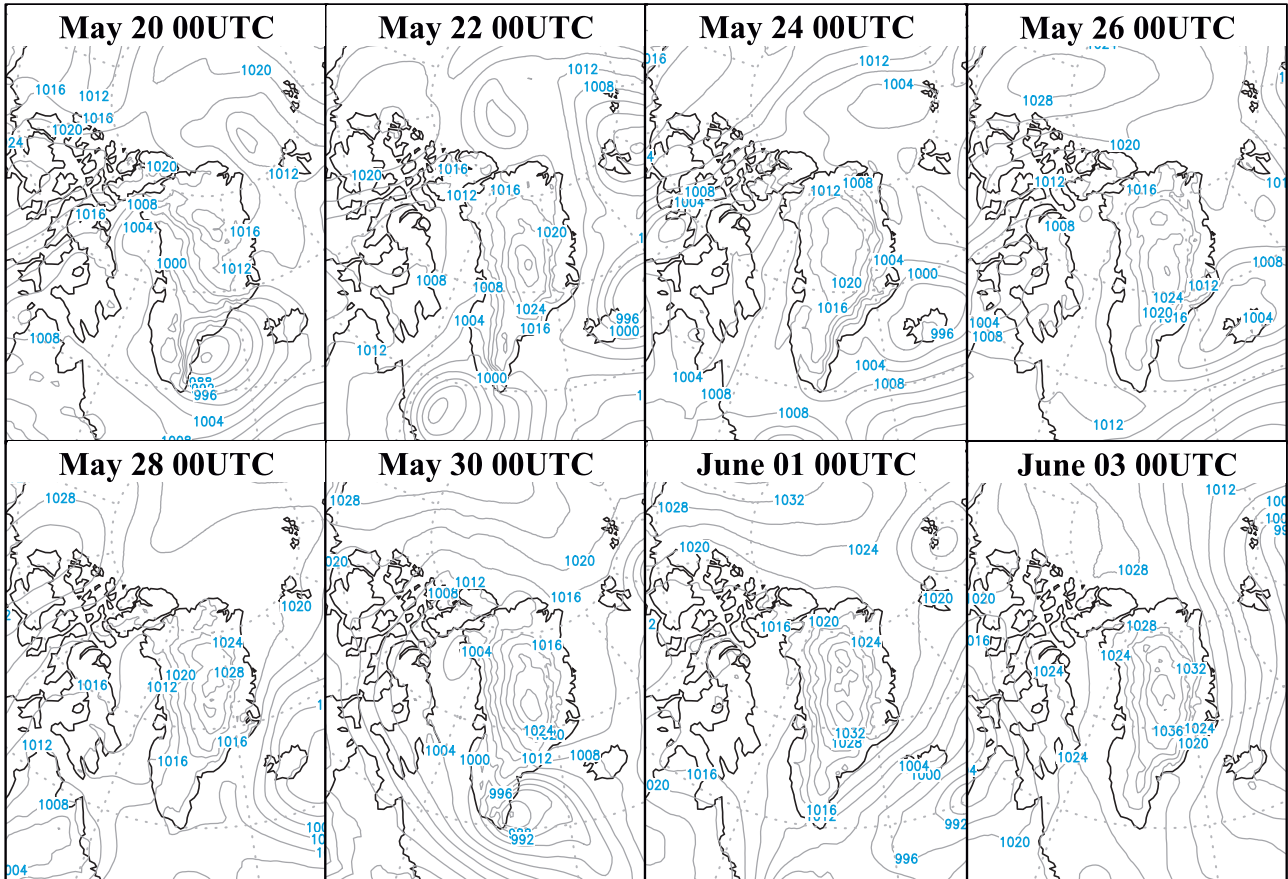


Figure 11 : Same as Fig. 10, but for the period ranging from May 20, 2015 through June 3, 2015.

and predicted downward shortwave radiant flux at SIGMA-A, the prediction of shortwave radiation worsened on cloudy days. In our model, cloud radiation was influenced by cloud formations determined by the amount of energy and water vapor within a grid volume of atmosphere, hence it is necessary to further validate our model with cloud fraction observations, such as an all-sky camera observation system, and to modify parameters related to the cloud microphysics and the cloud radiation process.

Compared with SIGMA-A, the performance of our local weather prediction system was considerably inferior at Bowdoin Glacier in terms of wind direction and surface air temperature. We note that the errors in predicted wind direction and surface air temperature tended to be larger when the observed wind speed was less than 5 m s^{-1} , as shown in Fig. 8. A possible explanation for this is as follows. When a large-scale environmental force is weak, the local air circulation near the surface is expected to be separate from large-scale winds, but more influenced by local effects, such as

topographic or thermodynamic effects from the surface. The topography and land surface characteristics around Bowdoin Glacier are entangled at a horizontal scale less than that of the grid spacing of our model, i.e., 5 km (Fig. 1 in Sugiyama et al., 2015), thus small-scale local air circulation patterns are not represented by our model.

In contrast, when the environmental force is stronger, surface air circulation is expected to be more affected by a large-scale wind that is resolvable with our model rather than by unresolvable local effects. Figure 12 shows that the pressure gradient over northwest Greenland increased from July 19, 2014 through July 21, 2014 in conjunction with a low pressure system approaching, which corresponds to the period in which our prediction showed good performance for wind direction, as shown in Fig. 6. Since a larger pressure gradient generally brings stronger winds, this synoptic scale feature in the focused period is consistent with the expectation that the accuracy of the predicted wind direction improves when a strong wind brought by a large-scale force is observed.

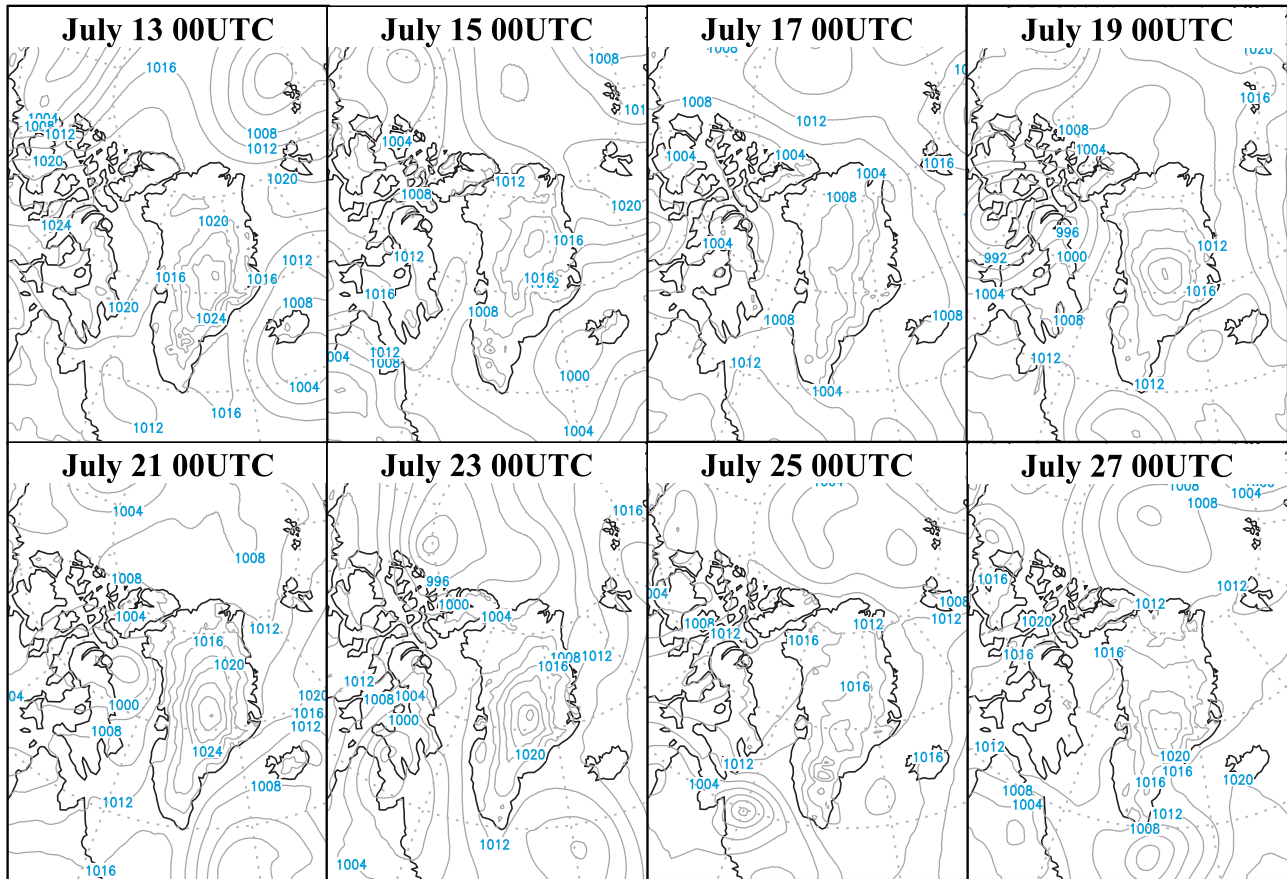


Figure 12 : Same as Fig. 10, but for the period ranging from July 13, 2014 through July 27, 2014.

Further, the surface air temperature is affected by both a local surface heat flux and a heat advection across a wide spatial range. For weaker winds, the air temperature is more influenced by the local surface heat flux, which includes sub-grid scale heterogeneity, due to topography and land surface characteristics; otherwise, it is more influenced by the large-scale heat advection resolvable with our model. Therefore, we can extend the same explanation for wind direction to surface air temperature. From the viewpoint of modeling, heat exchange at the land surface in a meteorological model is strongly dependent on the implemented land surface model and land surface characteristics, hence we need a high level of sophistication in the land surface model and a finer expression of topography and land surface characteristics to improve our prediction performance at Bowdoin Glacier.

7. Conclusions

In this paper, we described our efforts and results of

developing a weather prediction system based on JMA-NHM to support field research activities in Greenland with customized prediction information. Through feedback obtained from the expedition crews, we confirmed the effectiveness of our system in relation to field activities in terms of supporting scientific measurements and heliborne transportation. We updated our system during the selected campaigns by a collaboration between field and modeling researchers.

We validated our prediction results in relation to ground-based meteorological observation data collected at SIGMA-A, Bowdoin Glacier, and the SE-Dome during the field campaigns over the summer seasons from 2012 to 2015. Our system accurately predicted local weather parameters at these three sites, except for the downward shortwave radiation at SIGMA-A and the wind direction and surface air temperature at Bowdoin Glacier. To improve performance, our system needs to be improved in terms of its cloud radiation and land surface processes. We plan to maintain and refresh our system to support field activities in Greenland, including

those planned in upcoming projects named Post-SIGMA and the Arctic Challenge for Sustainability (ArCS).

In our paper, we also described the set up of our weather prediction system in Greenland. Our system can be extended for other weather prediction environments, including other Arctic or Antarctic regions, mountain glaciers, and so on according to available computational resource. In addition, Niwano et al. (2016) are currently attempting to perform climate simulations by a coupled model constructed by our system and the physical snowpack model SMAP (Snow Metamorphism and Albedo Process) applied in polar regions (Niwano et al., 2015). We believe such a system promotes more collaborative work among glaciologists and meteorologists to produce new and deeper understandings of the cryosphere-atmosphere system.

Acknowledgements

This work was partly supported by JSPS KAKENHI Grant Numbers JP16H01772, JP23221004, 26257201. The field observation campaign at Bowdoin Glacier was carried out under the Green Network of Excellence Program Arctic Climate Change Research Project. The ice core drilling campaign at the SE-Dome was carried out partly with the support of the Joint Research Program of the Institute of Low Temperature Science, Hokkaido University.

Appendix A

1. Errors of predicted parameters

The ME and RMSE of downward shortwave and longwave radiant fluxes are shown in Fig. A1 for the field campaigns at SIGMA-A. Figs. A2(a)–(d) show the ME and RMSE of wind speed, wind direction, surface air temperature and water vapor mixing ratio for the field campaigns at SIGMA-A, and (e)–(h) for the campaign at Bowdoin Glacier. Bar indicates RMSE. “n” indicates the sample number.

Appendix B

1. Downsized data

To provide an expedition team isolated from the Internet results of numerical weather prediction, from

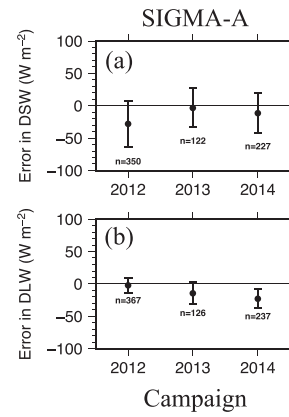


Figure A1 : The ME of (a) predicted downward shortwave radiant flux and (b) predicted downward longwave radiant flux. Bar indicates RMSE. “n” indicates the sample number.

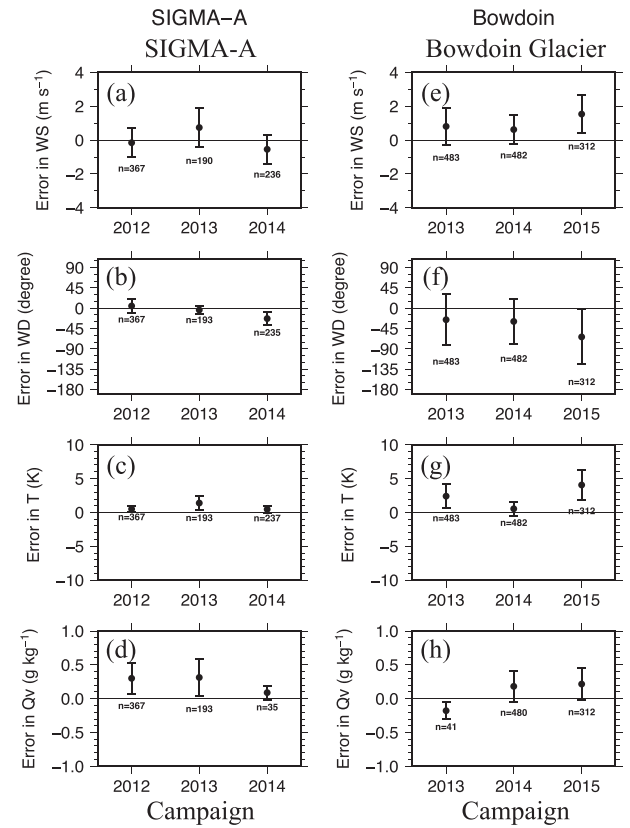


Figure A2 : The ME of (a) predicted wind speed, (b) predicted wind direction, (c) predicted surface air temperature and (d) predicted water vapor mixing ratio at SIGMA-A. (e)–(h) are same as (a)–(d), respectively, but for Bowdoin Glacier. Bar indicates RMSE. “n” indicates the sample number.

the output of each simulation, we extracted 10 meteorological parameters — i.e., air pressure, air temperature, humidity, cloud fractions of low, middle, and high layers, wind speed and direction, a rain/snow flag, and precipitation amount — at the surface and a height of 5 km a.s.l. at four predetermined locations, including the

Table B1 : Specifications of the downsized data, reproduced from Hashimoto et al. (2016) with permission.

	VARIABLE	UNIT	MIN	MAX	INCREMENT	TONE	SIZE	DIGIT
Station ID	VAR 0 ^U	(height) km	0	15	1	16	upper 4 bits	DIG 0 ^U
	VAR 0 _L		0	15	1	16	lower 4 bits	DIG 0 _L
Time	VAR 1	*day UTC	0	63.75	0.25	256	full 8 bits	DIG 1
Pressure	VAR 2	hPa	100	1120	4	256	full 8 bits	DIG 2
Temperature	VAR 3	°C	-100	27.5	0.5	256	full 8 bits	DIG 3
Humidity	VAR 4 ^U	%	25	100	5	16	upper 4 bits	DIG 4 ^U
High-cloud coverage	VAR 4 _L		0	1	0.0625	16	lower 4 bits	DIG 4 _L
Middle-cloud coverage	VAR 5 ^U		0	1	0.0625	16	upper 4 bits	DIG 5 ^U
Low-cloud coverage	VAR 5 _L		0	1	0.0625	16	lower 4 bits	DIG 5 _L
Wind velocity scale	VAR 6 ^U		0	15	1	16	upper 4 bits	DIG 6 ^U
16-direction wind scale	VAR 6 _L		0	15	1	16	lower 4 bits	DIG 6 _L
Flag (if snow < rain)	VAR 7 ^U		0	1	1	2	upper 1 bit	DIG 7 ^U
Precipitation scale	VAR 7 _L		0	5.1	0.04	128	lower 7 bits	DIG 7 _L

camp site, up to four times every 12 hours (i.e., 6, 18, 30, and 42 hours after the initial time). The output eight-byte datum of each parameter is then converted to a sub-byte datum via tone scale processing. After this processing is complete, the total data size, including the extracted data, the station ID, and the forecast time, is downsized to approximately one-tenth the original size, i.e., only 256 bytes.

Using the above algorithm, we converted and transmitted the downsized data through the satellite communication system to the expedition team. These transmitted data are then converted to their original values by applying the following:

$$VARn_L^U = MINn_L^U + \frac{DIGn_L^U}{TONE n_L^U - 1} (MAXn_L^U - MINn_L^U),$$

$$(n_L^U = 0^U, 0_L, 1, 2, 3, 4^U, 4_L, 5^U, 5_L, 6^U, 6_L, 7^U, 7_L) \quad (B1)$$

Here, $VARn_L^U$ represents the locations, forecast times, and the 10 meteorological parameters (i.e., eight-byte data), while $DIGn_L^U$ represents the downsized data. Further, $DIGN$ represents an integer datum with a one-byte length; $DIGN^U$ and $DIGN_L$ represent the upper four bits (upper one bit for $n=7$) and the lower four bits (lower seven bits for $n=7$), respectively, within $DIGN$. Finally, $MINn_L^U$, $MAXn_L^U$, and $TONE n_L^U$ represent the maximum and minimum values of $VARn_L^U$ and the number of tones, respectively. Specific values for these parameters are listed in Table B1.

References

- Aoki, T., S. Matoba, J. Uetake, N. Takeuchi, and H. Motoyama (2014) Field activities of the "Snow Impurity and Glacier Microbe effects on abrupt warming in the Arctic" (SIGMA) Project in Greenland in 2011–2013. *Bull. Glaciol. Res.*, **32**, 3–20, doi: 10.5331/bgr32.3.
- Bamber, J., S. Ekholm, and W. Krabill (2001), A new, high resolution digital elevation model of Greenland fully validated with airborne laser altimeter data. *J. Geophys. Res.*, **106**, 6733–6745.
- Bromwich, D. H., A. J. Monaghan, K. W. Manning, and J. G. Powers (2005) Real-time forecasting for the Antarctic: An evaluation of the Antarctic Mesoscale Prediction System (AMPS). *Mon. Wea. Rev.*, **133**, 579–603.
- Bromwich, D. H., F. O. Otieno, K. M. Hines, K. W. Manning, and E. Shilo (2013) Comprehensive evaluation of polar weather research and of forecasting performance in the Antarctic. *J. Geophys. Res.*, **118**, 274–292, doi: 10.1029/2012JD018139.
- Hara, T., 2008: Prediction of land surface quantities. The JMA Nonhydrostatic Model II, *Japan Meteorological Agency Annual Rep.*, **54**, 176–180. (in Japanese)
- Hara, K., S. Matoba, and T. Yamasaki (2014) Aerosol measurements at Siorapaluk, Greenland, The Fifth Symposium on Polar Science, Tokyo, 2–5 December 2014. http://www.nipr.ac.jp/symposium2014/program/abstract/OM_Hara_00355_01.pdf
- Hashimoto A., M. Murakami, T. Kato and M. Nakamura (2007) Evaluation of the Influence of Saturation Adjustment with Respect to Ice on Meso-scale Model Simulations for the Case of 22 June, 2002. *SOLA*, **3**, 085–088, doi: 10.2151/sola.2007-022.
- Hashimoto, A., M. Niwano, and T. Aoki (2016) Numerical weather prediction supporting cryospheric field observa-

- tion campaign on the Greenland Ice Sheet. *Seppyo*, **78**, 205–214. (in Japanese with English abstract)
- Hines, K. M., and D. H. Bromwich (2008) Development and Testing of Polar WRF. Part I. Greenland Ice Sheet Meteorology. *Mon. Wea. Rev.*, **136**, 1971–1989, doi: 10.1175/2007MWR2112.1.
- Hines, K. M., D. H. Bromwich, L.-S. Bai, M. Barlage, and A. G. Slater (2011) Development and testing of Polar WRF. Part III. Arctic land. *J. Clim.*, **24**, 26–48, doi: 10.1175/2010JCLI3460.1.
- Iizuka, Y., S. Matoba, T. Yamasaki, I. Oyabu, M. Kadota, and T. Aoki (2016) Glaciological and meteorological observations at the SE-Dome site, southeastern Greenland Ice Sheet. *Bull. Glaciol. Res.*, **33**, doi: 10.5331/bgr.15R03.
- Matoba, S., K. Hara, and T. Yamasaki (2014) Chemical compositions of frost flower at Siorapaluk in northwestern Greenland. The Fifth Symposium on Polar Science, Tokyo, 2–5 December 2014. http://www.nipr.ac.jp/symposium2014/program/abstract/OM_Matoba_00172_01.pdf
- Niwano, M., T. Aoki, S. Matoba, S. Yamaguchi, T. Tanikawa, K. Kuchiki, and H. Motoyama (2015) Numerical simulation of extreme snowmelt observed at the SIGMA-A site, northwest Greenland, during summer 2012. *The Cryosphere*, **9**, 971–988, doi: 10.5194/tc-9-971-2015.
- Niwano, M., T. Aoki, A. Hashimoto, T. Tanikawa, M. Hosaka, M. Hori, R. Shimada, S. Matoba, S. Yamaguchi, K. Fujita, and H. Motoyama (2016) Initial evaluation of the NHM-SMAP regional climate model in the Greenland ice sheet during 2012. JSSI & JSSE Joint Conference, Nagoya, 28 September to 2 October 2016. (in Japanese)
- Powers, J. G., A. J. Monaghan, A. M. Cayette, D. H. Bromwich, Y.-H. Kuo, and K. W. Manning (2003) Real-time mesoscale modeling over Antarctica: The Antarctic Mesoscale Prediction System (AMPS). *Bull. Amer. Meteor. Soc.*, **84**, 1533–1545, doi: 10.1175/BAMS-84-11-1533.
- Saito K, T. Fujita, Y. Yamada, J. Ishida, Y. Kumagai, K. Aranami, S. Ohmori, R. Nagasawa, S. Kumagai, C. Muroi, T. Kato, H. Eito, Y. Yamazaki (2006) The Operational JMA Nonhydrostatic Mesoscale Model. *Mon. Wea. Rev.*, **134**, 1266–1297.
- Sugiyama, S., D. Sakakibara, S. Tsutaki, M. Maruyama, and T. Sawagaki (2015) Glacier dynamics near the calving front of Bowdoin Glacier, northwestern Greenland. *J. Glaciol.*, **61**, 223–232, doi: 10.3189/2015JoG14J127.
- Tao, W.-K., J. Simpson, and M. McCumber (1989) An ice-water saturation adjustment. *Mon. Wea. Rev.*, **117**, 231–235.
- Wilson, A. B., D. H. Bromwich, K. M. Hines (2011) Evaluation of Polar WRF forecasts on the Arctic System Reanalysis domain: Surface and upper air analysis. *J. Geophys. Res.*, **116**, D11112, doi: 10.1029/2010JD015013.